# Corrosion properties of ECAP-processed Mg−Al−Ca−Mn alloys with separate Al$_2$Ca and Mg$_2$Ca phases

Shu-heng HE[1], Ce WANG[2], Chao SUN[1], Yue ZHANG[3], Kai YAN[4],
Jing-hua JIANG[1], Jing BAI[3], Feng XUE[3], Huan LIU[1,5]

1. College of Mechanics and Materials, Hohai University, Nanjing 210000, China;
2. School of Materials Science and Engineering, Tianjin University, Tianjin 300350, China;
3. School of Materials Science and Engineering, Southeast University, Nanjing 211189, China;
4. School of Mechanical Engineering, Yangzhou University, Yangzhou 225127, China;
5. Jiangsu Key Laboratory for Light Metal Alloys, Nanjing Yunhai Special Metals Co., Ltd., Nanjing 211200, China

**Abstract:** To investigate the effect of separate Al$_2$Ca and Mg$_2$Ca phases on the corrosion properties of Mg−Al−Ca−Mn alloys, OM, SEM, immersion and electrochemical tests were conducted on the as-cast and ECAP Al$_2$Ca-containing (2Ca) and Mg$_2$Ca-containing (4Ca) alloys. At the beginning of corrosion, the two as-cast alloys are corroded slowly compared with ECAP alloys. With prolonging the corrosion time, the corrosion of ECAP alloys becomes slighter than that of as-cast alloys, which is mainly ascribed to the dispersion and refinement of the second phase in ECAP alloys. Moreover, the corrosion degree of 2Ca alloys is always slighter than that of 4Ca alloys, suggesting that Al$_2$Ca phase is more beneficial to the enhancement of corrosion resistance of Mg−Al−Ca−Mn based alloys than Mg$_2$Ca phase. Finally, based on the examinations of corrosion surface and electrochemical testing results, different corrosion mechanisms caused by the distributions and morphology of Al$_2$Ca and Mg$_2$Ca phases are discussed.
**Key words:** Mg−Al−Ca−Mn alloy; equal channel angular pressing; second phase; refinement; corrosion properties

## 1 Introduction

Magnesium (Mg) alloys have been considered as an important lightweight structural material owing to their low density, high specific stiffness, good electrical conductivity, electromagnetic shielding performance, easy application and recovery [1−5]. However, the corrosion resistance of Mg alloys is very poor, which greatly limits their commercial applications, especially in corrosive environments such as seawater [6−9]. Although the addition of rare earth (RE) elements can improve corrosion resistance of magnesium alloys [10−12], it will greatly increase the cost and density of Mg alloys, which is an impediment to large-scale industrial applications. Therefore, it is necessary to develop RE-free Mg alloys with synergistic good mechanical properties and corrosion resistance.

Mg−Al−Ca−Mn based alloys are one kind of new generation Mg alloys with a wide application prospect [13−17]. Al element could make Mg alloys form an oxide layer containing Al$_2$O$_3$, which exhibits better protective effect than MgO and thereby improves the corrosion properties of Mg alloys [18,19]. The addition of Mn element could introduce grain refinement and enhance magnesium alloys [20,21]. Moreover, Mn could also reduce the content of impurities in magnesium alloys [22], and improve the stability of the surface layer [23],

thereby improving the corrosion resistance of Mg alloys. With regard to Ca element, its addition in Mg alloys could inhibit the formation of $Mg_{17}Al_{12}$ phase [24,25]. YANG et al [24] studied the effect of Ca addition on the corrosion behavior of Mg−Al−Mn alloys, and found that when the content of Ca was 2 wt.%, the alloy showed the best corrosion resistance. This phenomenon was attributed to a large number of discontinuous $(Mg,Al)_2Ca$ phases, which acted as a sacrificial anode to protect the Mg matrix. KIM et al [26] studied the corrosion behavior of Mg−5Al-based alloy with the addition of Ca lower than 2 wt.%, and found that the second phases ($Al_2Ca$ and $Mg_2Ca$) were the barrier which inhibited the corrosion of the matrix of the alloy. However, the effect of different contents of Ca on the corrosion resistance of Mg−Al−Ca−Mn alloys remains elusive.

Equal channel angular pressing (ECAP) is one of the most commonly used effective methods for preparing ultra-fine grained (UFG) metallic materials. By increasing the passes of ECAP, large deformation strains can be generated without changing the shape of the sample [27,28]. In the past twenty years, ECAP has been performed on various Mg alloys, and the results show that multi-pass ECAP can effectively refine the bulk or network second phase, such as $Mg_{17}Al_{12}$ phase [29], $Mg_2Si$ particle [30] and LPSO phase [31,32]. By refining these hard second phases, a uniform microstructure with scattered broken particles and $\alpha$-Mg grains was obtained, which could significantly improve the mechanical properties and corrosion resistance of the alloys [31,33−35]. Up to date, however, less studies have been reported on the effect of ECAP on the corrosion resistance of Mg−Al−Ca-based alloys.

Based on the above considerations, an Mg−3.7Al−1.8Ca−0.4Mn alloy with a single $Al_2Ca$ second phase and an Mg−3.7Al−4.5Ca−0.4Mn alloy (wt.%) with a single $Mg_2Ca$ second phase were prepared in this study. First, the effect of different second phases on the corrosion resistance of the alloys and the underlying mechanisms were studied. Second, the effect of ECAP on the mechanical and corrosion properties of two Mg−Al−Ca−Mn alloys was studied and analyzed by comparing the corrosion properties of as-cast and ECAP alloys.

## 2 Experimental

In this study, the Mg−3.7Al−1.8Ca−0.4Mn and Mg−3.7Al−4.5Ca−0.4Mn alloys were prepared by semi-continuous casting from pure Mg, pure Al, Mg−30Ca (wt.%), and Mg−10Mn (wt.%) master alloys in an electric resistance furnace under the protection of $CO_2$ (99 vol.%) and $SF_6$ (1 vol.%) mixed gas. The ECAP samples with a size of 50 mm × 50 mm × 100 mm were cut from the ingots, and then rotary-die (RD) ECAP processing was employed to produce refined and homogeneous alloys for further investigation. The RD-ECAP was performed in a mold with four cross channels [36], and the aperture size was 50 mm × 50 mm. The as-cast samples were ECAP processed at 350 °C for 32 passes, and after every 12 passes, both the sample and rotary die were reheated in an electromagnetic induction furnace for 15 min. Hereafter, the four alloys are denoted as 2Ca-cast, 4Ca-cast, 2Ca-ECAP, and 4Ca-ECAP alloys, respectively.

After grinding and polishing, the metallographic samples were etched by the alcohol solution with a volume fraction of 4% nitric acid. The microstructure of various samples was characterized using the optical microscopy (OM, Olympus BX51 M) and scanning electron microscopy (SEM, Sirion 200). The tensile test at room temperature was carried out on a universal material testing machine (SUNS UTM4294X) at a tensile speed of $1\times10^{-3}\,s^{-1}$. For each alloy, the tensile test was repeated at least three times.

The corrosion rate of the alloy was evaluated by hydrogen evolution test. All samples were immersed in 3.5 wt.% NaCl aqueous solution (pH ~6.8) at 25 °C for 96 h. The hydrogen is collected by means of a burette attached to a funnel. The corrosion morphology of the four alloys was characterized by SEM. The corrosion rate $P_{AH}$ (mm/a) was obtained from hydrogen evolution by

$$P_{AH} = 2.088\Delta V/(A \cdot t) \tag{1}$$

where $\Delta V$ (mL) is the total volume of hydrogen evolved for the total immersion time, $A$ (cm$^2$) is the exposed surface area of the specimen, and $t$ (d) is the immersion time [37,38].

To investigate the corrosion mechanisms of

the studied alloys, two series of samples were selected for electrochemical experiments. One set was the samples without immersion (denoted as 0 h samples). The other set was those immersed in 3.5 wt.% NaCl aqueous solution for 30 h (denoted as 30 h samples). Electrochemical experiments were carried out with a three-electrode system in an aqueous solution containing 3.5 wt.% NaCl at 25 °C. The saturated calomel electrode (SCE) and platinum foil were used as the reference electrode and the counter electrode, respectively, and the exposed surface area of 1 cm$^2$ was the working electrode. Electrochemical impedance spectroscopy (EIS) measurements were carried out at a voltage amplitude of 5 mV and a frequency range from 100 kHz to 0.01 Hz. The potential of −1.9 V (vs SCE) and −1.2 V (vs SCE) was scanned at a scanning rate of 1 mV/s to obtain the dynamic potential polarization curve. Prior to EIS and polarization measurements, the tested samples were immersed in the NaCl solution for around 1 h to obtain a stable OCP value. All these electrochemical tests were repeated at least three times to ensure good repeatability. Zsimpwin software was used to analyze the collected data.

## 3 Results and discussion

### 3.1 Microstructure of studied alloys

Figure 1 shows the microstructures of two as-cast alloys. The optical images of Figs. 1(a, c) indicate that both alloys are composed of $\alpha$-Mg matrix and continuous second phase at the grain boundaries. Measured by Image-J software, the area fraction of the second phase is estimated to be 12% and 16% for 2Ca-cast and 4Ca-cast alloys, respectively. The SEM images (Figs. 1(b, d)) reveal that there are also some cubic particles distributed at or near the network phase. Based on previous EDS analysis [39], Region A in 2Ca-cast alloy with higher Al and Ca contents is the eutectic structure composed of Al$_2$Ca phase and $\alpha$-Mg matrix. However, Region B containing high contents of Mn and Al elements is Al$_8$Mn$_5$ phase. Similarly, Region C in 4Ca-cast alloy is confirmed to be Mg$_2$Ca phase and $\alpha$-Mg eutectic structure, and cubic particle of Region D is also Al$_8$Mn$_5$ phase, which are consistent with our previous characterizations [40].

Figure 2 shows the microstructures of two alloys after ECAP. As can be seen from the OM image (Fig. 2(a)), the network eutectic phases originally located at grain boundaries are obviously broken and dispersed, although the slight streamline distribution of broken particles can still be observed. Moreover, under the combined action of high temperature and stress, dynamic recrystallization (DRX) occurs in the originally coarse $\alpha$-Mg grain, resulting in the formation of a large number of uniformly distributed fine grains. From the high-magnification SEM images (Fig. 2(b) and its inset), it can be seen that the broken Al$_2$Ca phase presents a spherical shape after ECAP, which has been
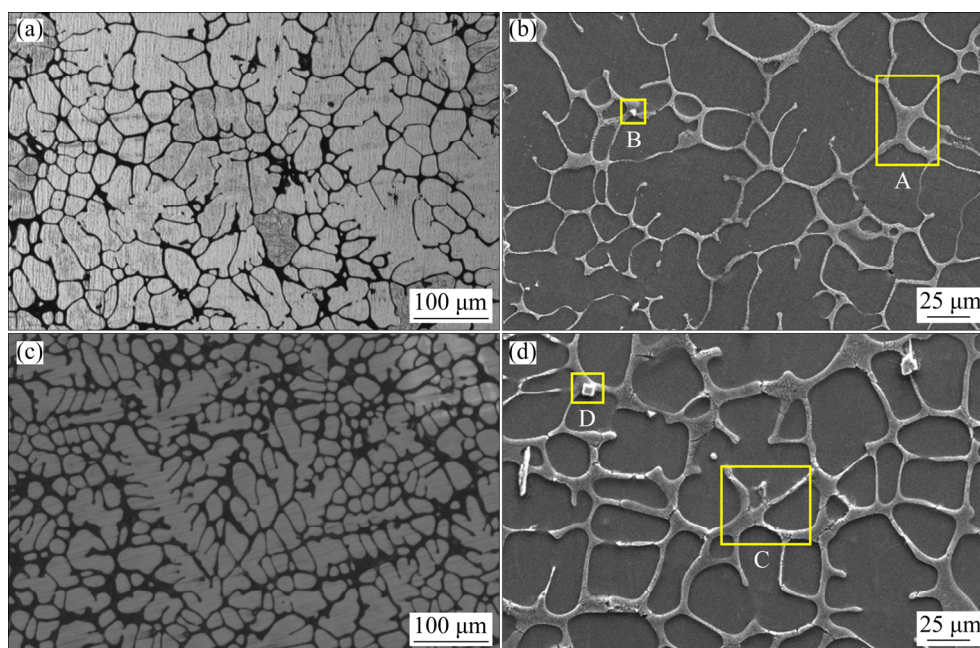


**Fig. 1** Optical micrographs (a, c) and SEM micrographs (b, d) of 2Ca-cast (a, b) and 4Ca-cast (c, d) alloys
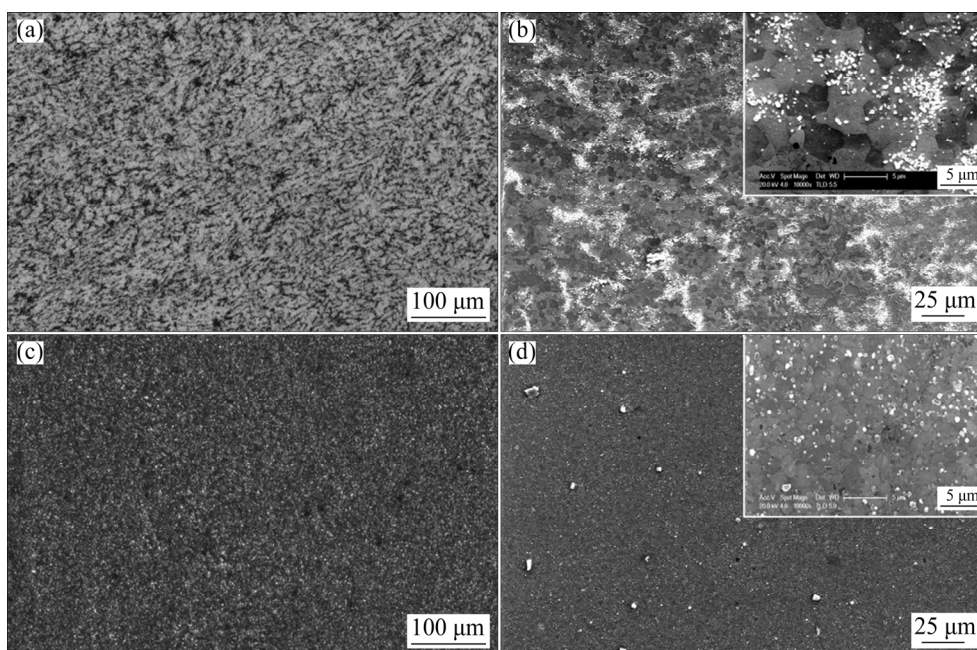
**Fig. 2** Optical micrographs (a, c) and SEM micrographs (b, d) of 2Ca-ECAP (a, b) and 4Ca-ECAP (c, d) alloys

refined and dispersed efficiently, but with partial aggregation at grain boundaries. Moreover, the sizes of them are in the range of 0.2−0.4 μm, while the average grain size of $\alpha$-Mg is estimated to be 4.1 μm.

Figures 2(c, d) show the OM and SEM microstructures of 4Ca-ECAP alloy. As can be seen from Fig. 2(c), eutectic phase originally distributing at the grain boundary is fragmented into fine particles and uniformly dispersed. SEM images (Fig. 2(d) and its inset) show that the $Mg_2Ca$ particles are uniformly dispersed with an average particle size of 0.3 μm. The 4Ca-ECAP alloy displays a complete DRX microstructure with an average grain size of 2.4 μm. Moreover, most $Mg_2Ca$ particles are located at grain boundaries, which could hinder the growth of DRX grains.

### 3.2 Mechanical properties

Figure 3 and Table 1 show the typical tensile curves and mechanical properties of the studied alloys, respectively. It is apparent that the comprehensive mechanical properties of the two alloys are greatly improved after ECAP. The 2Ca-ECAP alloy exhibits lower YS but higher UTS and EL (reaching 20%) compared with the 4Ca-ECAP alloy. The excellent mechanical properties of the alloys after ECAP are mainly due to grain refinement and the dispersion of refined
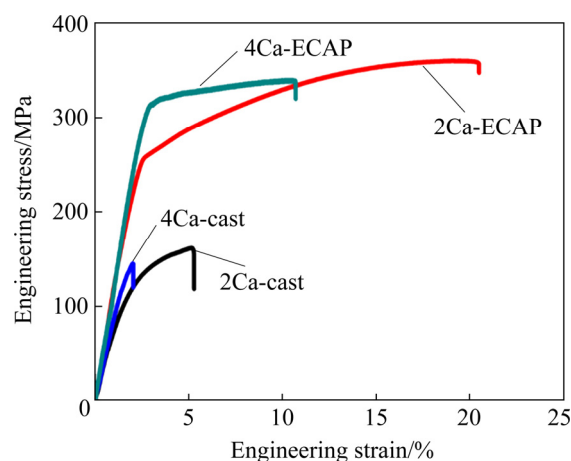


**Fig. 3** Typical tensile curves of studied alloys

**Table 1** Tensile yield strength (YS), ultimate tensile strength (UTS) and fracture elongation (EL) of Mg−Al−Ca−Mn alloys

| Alloy | YS/MPa | UTS/MPa | EL/% |
|---|---|---|---|
| 2Ca-cast | 71 | 161 | 5.1 |
| 4Ca-cast | 102 | 118 | 2.7 |
| 2Ca-ECAP | 252 | 360 | 20.5 |
| 4Ca-ECAP | 296 | 339 | 11 |

second phase particles. Moreover, the dispersion of second phase could reduce the stress concentration, crack initiation and propagation during tensile testing, thus improving the ductility of the alloy prominently [41].

## 3.3 Corrosion behaviors

### 3.3.1 Immersion test results

Figure 4 shows the hydrogen evolution results of the studied alloys immersed in 3.5 wt.% NaCl solution for the first 12 and 96 h. The volume of hydrogen evolution gradually increases with the extension of immersion time. In the first 12 h, the volumes of hydrogen evolution of ECAP alloys are significantly higher than those of as-cast alloys with the same alloy compositions.
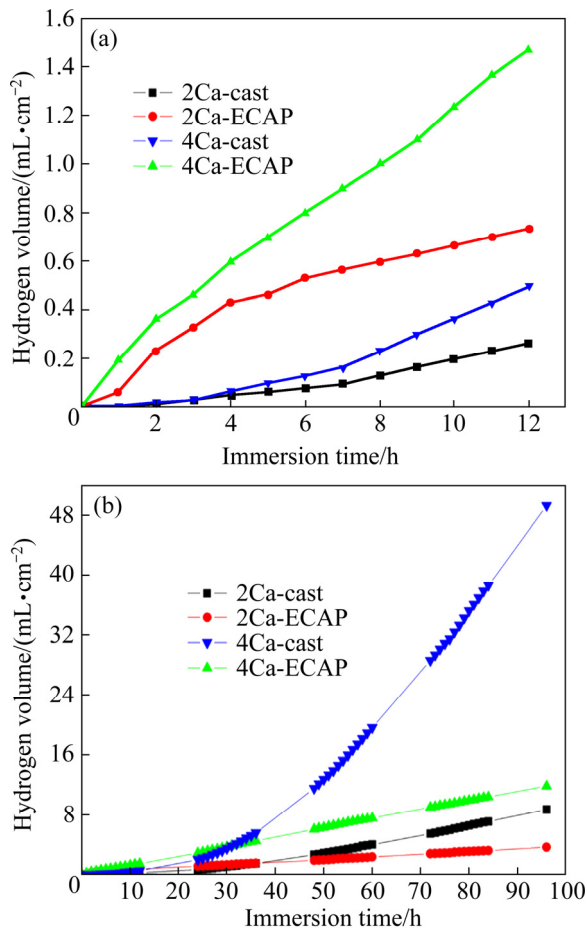


**Fig. 4** Hydrogen evolution volumes of studied alloys immersed in 3.5 wt.% NaCl solution for 12 h (a) and 96 h (b)

However, with the prolonging of immersion time, the volumes of hydrogen evolution of the as-cast alloys gradually exceed those of the ECAP alloys. The slopes of the curves for the as-cast alloys increase rapidly, suggesting that the corrosion resistances of them become weaker. In particular, the volume of hydrogen evolution for the 4Ca-cast alloy begins to surge after 30 h, reaching the highest (49.3 mL/cm$^2$) after being immersed for 96 h. As for the 2Ca-cast alloy immersed for 96 h, it

is only 8.7 mL/cm$^2$. The hydrogen volume variation of 2Ca-ECAP and 4Ca-ECAP alloys is similar, showing a steady rising trend. After 96 h of immersion, the volumes of hydrogen evolution for two ECAP alloys are only 3.63 and 11.83 mL/cm$^2$, respectively. Therefore, ECAP alloys produce less hydrogen than as-cast alloys with longer immersion time. The detailed data for the average corrosion rates $P_{AH}$ of 12 and 96 h are presented in Table 2. It can be found that the $P_{AH}$ of ECAP alloys is higher than that of as-cast alloys after 12 h of immersion. However, 4Ca-cast has the highest $P_{AH}$ after 96 h of immersion. The $P_{AH}$ of 2Ca alloy is always lower than that of 4Ca alloy in the same state.

**Table 2** Corrosion rates ($P_{AH}$) calculated from hydrogen evolution rate after 12 h and 96 h of immersion test by using Eq. (1)

| Immersion time/h | Alloy | $\Delta V$/mL | $P_{AH}$/(mm·a$^{-1}$) |
|---|---|---|---|
| 12 | 2Ca-cast | 0.27 | 1.13 |
| | 2Ca-ECAP | 0.73 | 3.05 |
| | 4Ca-cast | 0.5 | 2.09 |
| | 4Ca-ECAP | 1.47 | 6.14 |
| 96 | 2Ca-cast | 8.7 | 4.54 |
| | 2Ca-ECAP | 3.63 | 1.89 |
| | 4Ca-cast | 49.3 | 25.74 |
| | 4Ca-ECAP | 11.83 | 6.18 |

The corrosion morphologies of the alloys immersed in 3.5 wt.% NaCl solution for 30 h after the removal of corrosion products are shown in Fig. 5. The surface of 2Ca-cast alloy is relatively uniform with the presence of many shallow corrosion grooves. Corrosion mainly occurs on the Mg matrix, while the second phase is not corroded. According to previous report [42], the Al$_2$Ca second phase has higher positive potential than the Mg substrate, which accelerates the corrosion of the nearby Mg substrate. As shown in Fig. 5(b), after immersion for 30 h, the corroded surface of 2Ca-ECAP alloy is rough, which may be caused by the shedding of the second phases around the substrate after the substrate is dissolved.

As can be seen from Fig. 5(c), 4Ca-cast alloy has the most serious corrosion degree. A large number of deep pits are formed on the surface of the alloy, indicating a poor corrosion resistance. The deep pits may be resulted from the shedding of

Mg matrix after the dissolving of Mg$_2$Ca second phase, as Mg$_2$Ca phase shows more negative potential than Mg matrix [43]. Figure 5(d) shows that many small corrosion pits left by the corrosion of the second phase can be observed on the surface of 4Ca-ECAP alloy. Overall, the corrosion degree of 4Ca-ECAP is relatively slight.

With prolonging the immersion time, the corrosion gradually gets worse. It is apparent from Figs. 6(a, c) that serious corrosion occurs on two as-cast alloys after 96 h immersion. The corrosion pits are significantly deeper and larger than those after 30 h immersion, and the 4Ca-cast alloy is corroded most severely. Figures 6(b, d) show that
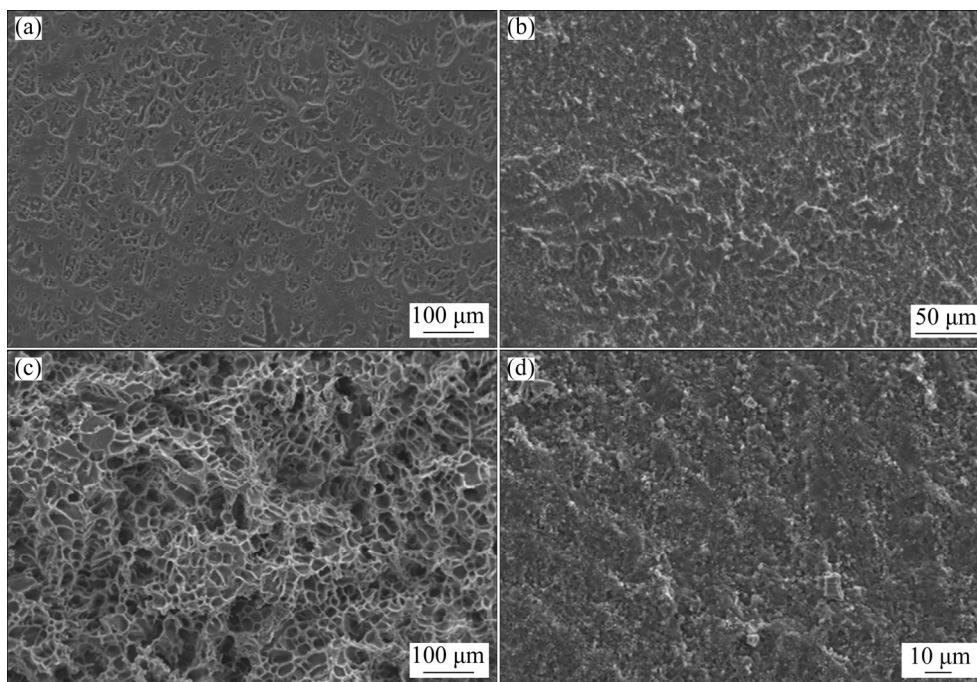


**Fig. 5** Corrosion morphologies of 2Ca-cast (a), 2Ca-ECAP (b), 4Ca-cast (c) and 4Ca-ECAP (d) alloys immersed in 3.5 wt.% NaCl solution for 30 h
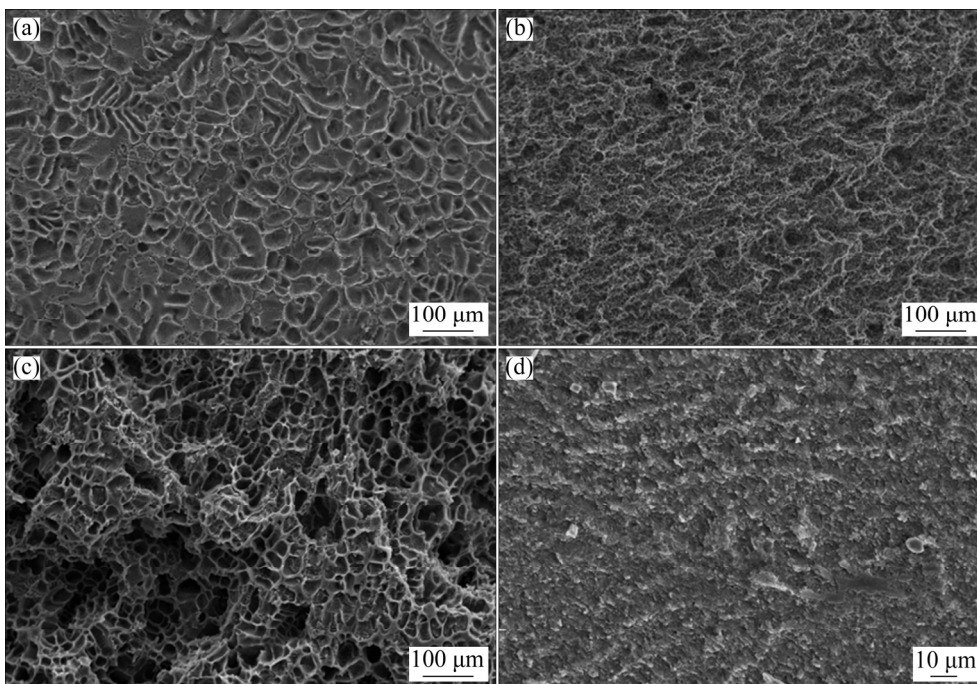


**Fig. 6** Corrosion morphologies of 2Ca-cast (a), 2Ca-ECAP (b), 4Ca-cast (c) and 4Ca-ECAP (d) alloys immersed in 3.5 wt.% NaCl solution for 96 h

the corrosion degree of the two ECAP alloys after 96 h immersion is significantly lighter than that of the as-cast alloys. Apparently, the corrosion resistance of ECAP alloys is better than that of as-cast alloys with prolonging the corrosion time. In general, the corrosion resistance of 2Ca alloy is better than that of 4Ca alloy.

### 3.3.2 Electrochemical test results

As the 30 h could be considered as the turning point for the increase of corrosion for as-cast alloys, 0 h and 30 h samples were then systematically investigated with electrochemical tests to explore the difference in corrosion behaviors between as-cast and ECAP alloys. Figure 7 shows the potentiodynamic polarization curves of as-cast and ECAP alloys at two series: 0 h and 30 h samples. The detailed electrochemical parameters extracted from the experimental results are given in Table 3. In general, the corrosion potential of the 0 h ECAP alloys is higher than that of the as-cast alloys. 4Ca-ECAP alloy has the highest $\varphi_{corr}$ (−1.531 V (vs SCE)), while 4Ca-cast alloy has the lowest $\varphi_{corr}$ (−1.548 V (vs SCE)). The corrosion current densities are evaluated from the corresponding polarization curves by Tafel extrapolation using the cathodic branches [44]. The $J_{corr}$ of the as-cast alloys is obviously lower than that of the ECAP alloys, indicating that the corrosion rate of the as-cast alloys is slower at the beginning. In addition, the anodic polarization curves show that both of the as-cast and ECAP alloys have no obvious passivation phenomenon.

As shown in Fig. 7(b), after being immersed for 30 h, the $\varphi_{corr}$ of both as-cast and ECAP alloys become higher (except 4Ca-ECAP). Surprisingly, the $J_{corr}$ of the as-cast alloys increases significantly, while the $J_{corr}$ of the ECAP alloys decreases. The $J_{corr}$ of the 4Ca-cast alloy is the highest, reaching 93.33 μA/cm², and the $J_{corr}$ of the 2Ca-ECAP alloy is the lowest, which is only 6.03 μA/cm². This shows that the corrosion resistance of ECAP alloys becomes better under long-term corrosion. Furthermore, the $J_{corr}$ of 2Ca alloy is always lower than that of 4Ca alloy.

The Nyquist plots, Bode plots and phase angle plots of the alloy obtained by electrochemical impedance spectroscopy (EIS) test are shown in Fig. 8. Nyquist plots of 0 h 2Ca-ECAP and 4Ca-ECAP alloys (Fig. 8(a)) are composed of large high-frequency capacity loops, small medium-
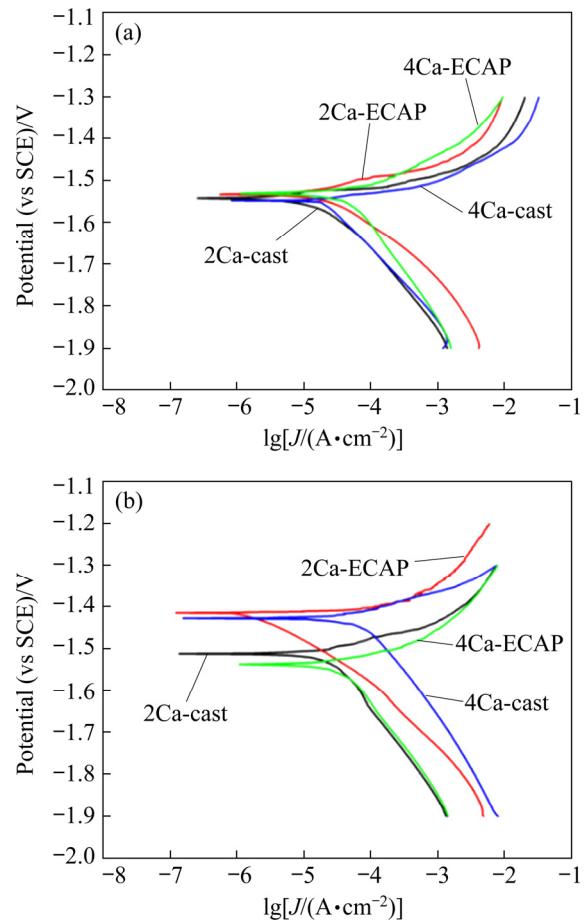


**Fig. 7** Potentiodynamic polarization curves of Mg−Al−Ca−Mn alloys: (a) 0 h samples; (b) 30 h samples

**Table 3** Corrosion potential ($\varphi_{corr}$) and corrosion current density ($J_{corr}$) of samples obtained from potentiodynamic polarization tests

| Immersion time/h | Alloy | $\varphi_{corr}$(vs SCE)/V | $J_{corr}$/ (μA·cm⁻²) |
|---|---|---|---|
| 0 | 2Ca-cast | −1.539 | 20.89 |
| | 2Ca-ECAP | −1.532 | 44.67 |
| | 4Ca-cast | −1.548 | 25.12 |
| | 4Ca-ECAP | −1.531 | 50.12 |
| 30 | 2Ca-cast | −1.512 | 22.91 |
| | 2Ca-ECAP | −1.417 | 6.03 |
| | 4Ca-cast | −1.425 | 93.33 |
| | 4Ca-ECAP | −1.536 | 33.88 |

frequency capacity loops and low-frequency induction loops. The as-cast alloys differ from the ECAP alloys with the absence of a low-frequency inductive loop. Moreover, the capacitive reactance arcs of as-cast alloys are obviously larger than that of ECAP alloys with the same alloy composition,
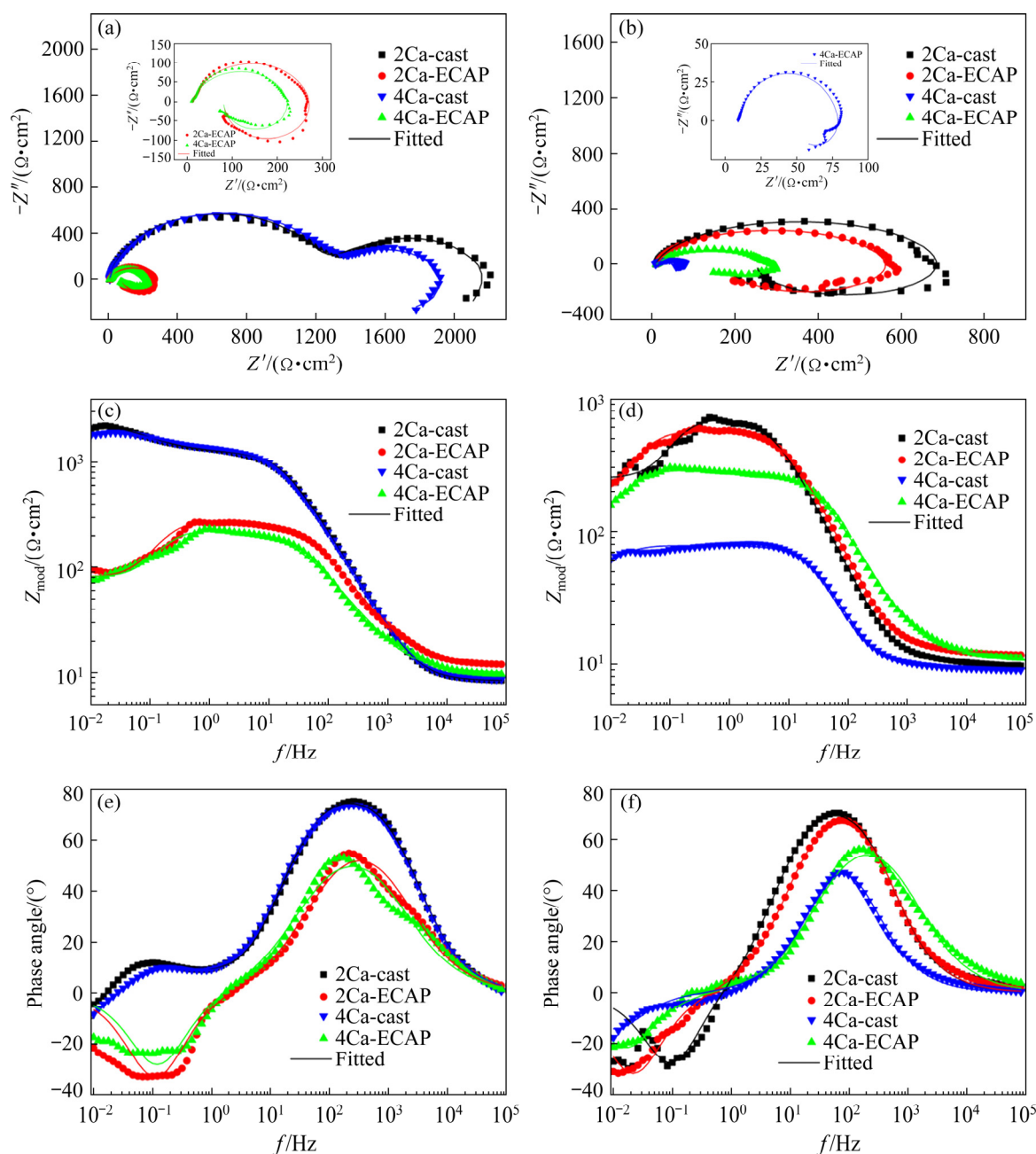
**Fig. 8** Impedance plots of Mg−Al−Ca−Mn alloys for 0 h samples (a, c, e) and 30 h samples (b, d, f): (a, b) Nyquist plots; (c, d) Bode plots; (e, f) Phase angle plots

and the capacitive reactance arc of 2Ca alloy is slightly larger than that of 4Ca alloy. As can be seen from Fig. 8(b), the Nyquist curves of the four alloys exhibit the same shape after being immersed for 30 h. The capacitive reactance arcs of as-cast alloys become significantly smaller, while those of ECAP alloys show negligible changes. Moreover, the capacitive reactance arc of 2Ca alloy is always larger than that of 4Ca alloy.

The Bode curve reflects the relationship between the impedance modulus and the frequency. It can be seen from Fig. 8(b) that the inflection

points on the Bode curves of 1 h samples correspond to the time constant observed in Nyquist plot. Impedance values vary significantly from 1 to 3 Hz, but change slightly at other frequencies. According to Nyquist plots, the maximum impedance of as-cast alloys is much higher than that of ECAP alloys with the same alloy composition, and the impedance of 2Ca alloy is slightly higher than that of 4Ca alloy. Figure 8(d) shows that after being immersed for 30 h, the impedance value of 4Ca-ECAP alloy is already higher than that of 4Ca-cast alloy, and the

impedance value of 2Ca alloy is still higher than that of 4Ca alloy.

The Bode phase angle reflects the relationship between angle and frequency. As shown in Fig. 8(e), the two as-cast alloys exhibit high-frequency wave crests and medium-frequency wave crests, which correspond to the large high-frequency capacity loops and small medium-frequency capacity loops in Fig. 8(a), respectively. As for the ECAP alloys, high-frequency wave crests, medium-frequency wave crests and wave troughs at low frequency are observed, consistent with the large high-frequency capacity loops, small medium-frequency capacity loops and low-frequency induction loops shown in Fig. 8(a), respectively. Furthermore, after being immersed for 30 h, 2Ca-cast alloy has wave trough at low frequency, while the other alloys have no wave trough (Fig. 8(f)).

In order to further analyze the corrosion mechanisms of the alloys, the corresponding equivalent circuit and EIS spectral fitting data are presented in Fig. 9 and Table 4, respectively. The fitting equivalent circuits corresponding to 2Ca-cast and 4Ca-cast 0 h samples are shown in Fig. 9(a), and the fitting equivalent circuits corresponding to other alloys are shown in Fig. 9(b).

$R_s$ is the solution resistance, while $R_{ct}$ and $CPE_{dl}$ describe the charge transfer resistance and electric double-layer capacitance in parallel. The $R_{ct}$ reflects the ability of the treated alloy to lose electrons. In addition, the higher the $R_{ct}$ value is, the more difficult it is to lose electrons, and the better the corrosion resistance is. The $CPE_{dl}$ is a constant phase element designed to represent the imperfect capacitance of two electrical layers due to the inhomogeneity of the electrochemical system. The oxide film resistor $R_f$ is parallel to the corresponding capacitor $CPE_f$ to reflect the surface oxidation behavior. The presence of $R_f$ in Fig. 9(a) indicates that the films of corrosion products provide some protection. And the absence of $R_f$ in the equivalent circuit corresponding to ECAP alloys is due to the lack of protection of the oxide film. CPE has a constant phase shift independent of frequency and can be defined by two values, $Y_{dl}$ and $n_{dl}$. If $n_{dl}$ is equal to 1, CPE is equal to a capacitor; if $n_{dl}$ is equal to 0, CPE is a resistor. $L$ and $R_L$ represent inductance and resistance, respectively, reflecting pitting of these alloys. The overall corrosion resistance of the alloys is represented by the sum of $R_{ct}$ and $R_f$. According to the data in Table 4, it can be found that the sum of $R_{ct}$ and $R_f$ of 0 h as-cast alloys is much higher than that of ECAP alloys, and the sum of $R_{ct}$ and $R_f$ of 2Ca alloy is higher than that of 4Ca alloy with the same alloy composition, indicating that the corrosion resistance of as-cast alloys and 2Ca alloy is better at the beginning of corrosion. After being immersed for
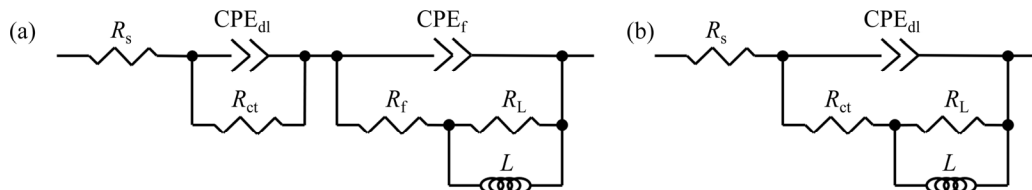


**Fig. 9** Equivalent circuits of EIS spectra: (a) 0 h 2Ca-cast and 4Ca-cast alloys; (b) All other states

**Table 4** Fitting results of EIS spectra

| Immersion time/h | Alloy | $R_s/\Omega$ | $Y_{dl}/$ $(s^n\cdot\Omega^{-1}\cdot cm^{-2})$ | $n_{dl}$ | $R_{ct}/$ $(\Omega\cdot cm^2)$ | $Y_f/$ $(s^n\cdot\Omega^{-1}\cdot cm^{-2})$ | $n_f$ | $R_f/$ $(\Omega\cdot cm^2)$ | $R_L/$ $(\Omega\cdot cm^2)$ | $L/H$ |
|---|---|---|---|---|---|---|---|---|---|---|
| 0 | 2Ca-cast | 8.431 | 0.0016 | 0.7065 | 1481 | 0.000011 | 0.9352 | 1211 | 111 | 33340 |
| | 2Ca-ECAP | 12.15 | 0.000037 | 0.8137 | 264.8 | | | | 93.39 | 237.3 |
| | 4Ca-cast | 8.619 | 0.000013 | 0.9197 | 1259 | 0.0016 | 0.7571 | 731.6 | 200.1 | 17010 |
| | 4Ca-ECAP | 10.06 | 0.00007 | 0.7837 | 218.8 | | | | 105 | 249.4 |
| 30 | 2Ca-cast | 10.29 | 0.0000053 | 0.9196 | 695.4 | | | | 371.5 | 1053 |
| | 2Ca-ECAP | 12.39 | 0.000044 | 0.9178 | 555.2 | | | | 230.4 | 3183 |
| | 4Ca-cast | 9.429 | 0.00014 | 0.9212 | 69.62 | | | | 84.26 | 1763 |
| | 4Ca-ECAP | 11.74 | 0.0047 | 0.8307 | 278.1 | | | | 216.5 | 3264 |

30 h, there is no $R_f$ in the equivalent circuit of as-cast alloys, which may be due to the destruction of the oxide film. The $R_{ct}$ of 4Ca-ECAP is higher than that of 4Ca-cast, and the $R_{ct}$ of 2Ca-ECAP is only slightly smaller than that of 2Ca-cast, indicating that the corrosion resistance of ECAP alloys becomes better while that of as-cast alloys gets worse with a longer immersion time. Combined with the hydrogen evolution result, it is rational to believe that the 2Ca-ECAP might exhibit the highest $R_{ct}$ value after 90 h immersion. In addition, the $R_{ct}$ values of 2Ca alloys are always higher than those of 4Ca alloys, indicating a better corrosion resistance of 2Ca alloys.

## 3.4 Discussion

The type, distribution and quantity of the second phase exert a significant effect on the corrosion behavior of magnesium alloys [45]. In order to reveal the influence of $Mg_2Ca$ and $Al_2Ca$ second phases on the corrosion behaviors of Mg−Al−Ca−Mn alloys, the schematic diagrams of the corrosion process are illustrated in Fig. 10. Figure 10(a) illustrates that corrosion products act as a protective film preventing the corrosion of the solution. When the protective film is destroyed, the micro-galvanic couples are formed between the $Mg_2Ca$ phase and the $\alpha$-Mg matrix for 4Ca-cast alloy. Since the potential of $Mg_2Ca$ is lower than that of $\alpha$-Mg matrix, the $\alpha$-Mg matrix acts as the cathode and $Mg_2Ca$ phase acts as the anode to be corroded [43,46]. The corrosion penetrates rapidly along the grain boundaries, eventually leaving continuous corrosion channels. In this way, the $\alpha$-Mg matrix loses support and falls off in large quantities, which is confirmed by Fig. 6(c). Therefore, with the increase of immersion time, the corrosion of 4Ca-cast alloy becomes the most serious.

For 2Ca-cast alloy (Fig. 10(b)), the $\alpha$-Mg matrix is dissolved as an anode. At the same time, continuous $Al_2Ca$ phase acts as a barrier for protecting the $\alpha$-Mg matrix from corrosion, and the corrosion is limited [42,47]. Therefore, the corrosion resistance of 2Ca-cast alloy is better than that of 4Ca-cast alloy.

As shown in Fig. 10(c), due to the poor protection of the oxide film, the solution corrodes rapidly to the $\alpha$-Mg matrix. It can also be seen that $Mg_2Ca$ phase in 4Ca-ECAP alloy is largely dispersed after ECAP. Consequently, when the corrosion occurs, it does not penetrate along the grain boundary, and the propagation of corrosion is interrupted. Therefore, under long-term corrosion, the corrosion resistance of 4Ca-ECAP is obviously enhanced and becomes better than that of 4Ca-cast alloy. Since the corrosion happens within the $Mg_2Ca$ phase particles, and corrosion pits left by dissolution of $Mg_2Ca$ can be observed in Fig. 6(d).

When $Al_2Ca$ network is broken after ECAP, the dispersed $Al_2Ca$ particles in 2Ca-ECAP alloy form micro-galvanic couples with the surrounding $\alpha$-Mg matrix, and the $\alpha$-Mg matrix is dissolved (Fig. 10(d)). $Al_2Ca$ is separated from the matrix when the $\alpha$-Mg is completely dissolved. Compared with 4Ca-ECAP alloy, this corrosion mechanism causes more severe local corrosion. However, the corrosion resistance of 2Ca-ECAP alloy is better than that of 4Ca-ECAP alloy, which can be attributed to the content of the second phase. As reported in a previous reference [48], the higher the volume fraction of the second phase is, the worse the corrosion resistance is. Compared with 2Ca-ECAP alloy, 4Ca-ECAP alloy contains more secondary phases, and consequently more micro-galvanic couples are formed during the corrosion process. Compared with 2Ca-cast alloy, the corrosion resistance of 2Ca-ECAP alloy is further improved because of the dispersion and refinement of the second phase. First, since $Al_2Ca$ particles are dispersed in the $\alpha$-Mg matrix, the corrosion products are continuous, and the corrosion of $Cl^-$ is delayed, thereby forming a corrosion film with a certain protective ability [49]. Second, existing studies have shown that the current density between AZ91 magnesium alloy and other metals significantly reduces with decreasing the surface area ratio of cathode to anode [50,51]. When $Al_2Ca$ is dispersed and refined, the surface area ratio of $Al_2Ca$ to $\alpha$-Mg matrix becomes smaller, which weakens the corrosion of micro-galvanic couples between $Al_2Ca$ and $\alpha$-Mg matrix, thereby improving the corrosion resistance of Mg alloy under long-time immersion.

In addition, grain refinement also helps to improve the corrosion resistance by acting as physical corrosion barriers [52,53]. ECAP alloys have finer grains and thereby exhibit a better corrosion resistance under long-time corrosion. Nevertheless, according to Fig. 9(a), it can be seen
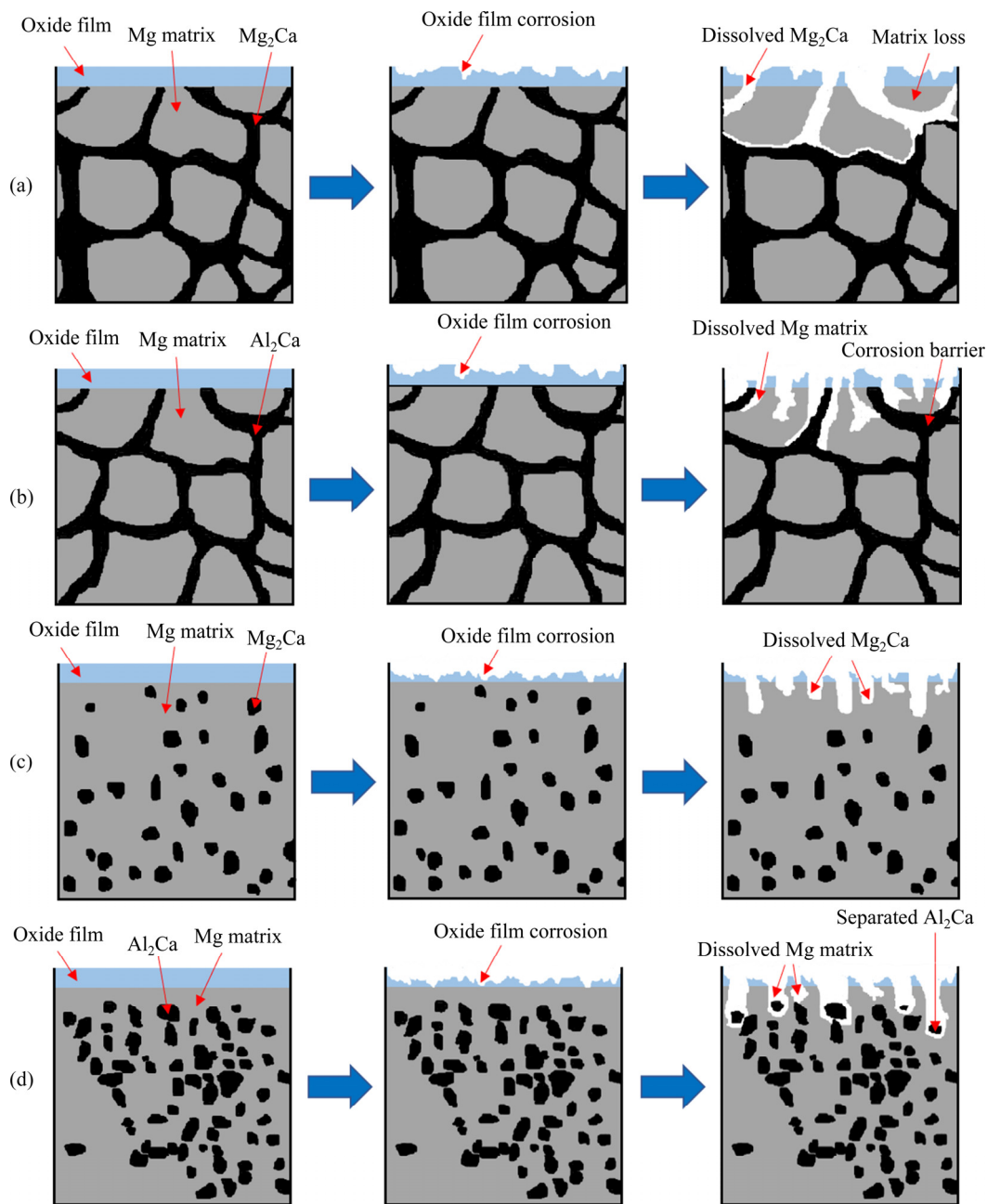
**Fig. 10** Schematic illustration of role of secondary phases in corrosion behavior of Mg−Al−Ca−Mn alloys: (a) 4Ca-cast; (b) 2Ca-cast; (c) 4Ca-ECAP; (d) 2Ca-ECAP

that the oxide film of the as-cast alloys provides a better protection. As a result, the corrosion resistance of as-cast alloys is better at the onset of corrosion. However, as the corrosion further proceeds, the oxide film is destroyed, and the corrosion begins to accelerate [54]. Other studies have shown that in a corrosive environment, small grains are prone to corrosion at the initial stage [55]. Therefore, compared with the ECAP alloys, the as-cast alloys are less prone to corrosion at the initial stage, while the ECAP alloys show a better corrosion resistance with prolonged corrosion time.

## 4 Conclusions

(1) Mg−3.7Al−1.8Ca−0.4Mn alloy is mainly composed of $\alpha$-Mg matrix and continuous network eutectic structure ($\alpha$-Mg+Al$_2$Ca) at the grain boundaries, while Mg−3.7Al−4.5Ca−0.4Mn alloy consists of $\alpha$-Mg and $\alpha$-Mg+Mg$_2$Ca networked eutectic structure. The microstructure of both alloys is obviously refined after 32 passes of ECAP, and the second phases are broken and dispersed. Moreover, the comprehensive mechanical properties

of the alloys are greatly improved.

(2) At the beginning of immersion, the corrosion rates of ECAP alloys are faster. But the corrosion of as-cast alloys becomes worse with prolonging the immersion time to 30 h. After 96 h of immersion, the ECAP alloys show lower corrosion rates. Moreover, the 2Ca alloy always exhibits a higher corrosion resistance than the 4Ca alloy.

(3) The as-cast alloys are less prone to corrosion at the initial stage because the oxidation films formed on as-cast alloys are relatively protective. As the corrosion proceeds, the oxide films are destroyed and then the corrosion begins to accelerate. The continuous distribution of $Mg_2Ca$ phase as the anode leads to the worse corrosion resistance, while the $Al_2Ca$ distributed continuously along grain boundaries could be considered as a corrosion barrier to protect the matrix. After ECAP, the second phases in the alloys are obviously dispersed and refined, which greatly improves the corrosion resistance of the alloys under long-time corrosion.

## Acknowledgments

## References

[1]     XU Shi-yuan, LIU Chu-ming, WAN Ying-chun, ZENG Guang, GAO Yong-hao, JIANG Shu-nong. Corrosion behaviour of Mg−Gd−Y−Zn−Ag alloy components with different sizes after cooling [J]. Transactions of Nonferrous Metals Society of China, 2021, 31: 1291−1302.

[2]     BAZHENOV V E, SAIDOV S S, TSELOVALNIK Y V, VOROPAEVA O O, PLISETSKAYA I V, TOKAR A A, BAZLOV A I, BAUTIN V A, KOMISSAROV A A, KOLTYGIN A V, BELOV V D. Comparison of castability, mechanical, and corrosion properties of Mg−Zn−Y−Zr alloys containing LPSO and W phases [J]. Transactions of Nonferrous Metals Society of China, 2021, 31: 1276−1290.

[3]     QIU Zai-meng, ZENG Rong-chang, ZHANG Fen, SONG Liang, LI Shuo-qi. Corrosion resistance of Mg−Al LDH/

[4]     CAO Fu-yong, ZHANG Jing, LI Ke-ke, SONG Guang-ling. Influence of heat treatment on corrosion behavior of hot rolled $Mg_5Gd$ alloys [J]. Transactions of Nonferrous Metals Society of China, 2021, 31: 939−951.

[5]     CHEN Jia-ling, FANG Liang, WU Fang, ZENG Xian-guang, HU Jia, ZHANG Shu-fang, JIANG Bin, LUO Hai-jun. Comparison of corrosion resistance of MgAl−LDH and ZnAl−LDH films intercalated with organic anions ASP on AZ31 Mg alloys [J]. Transactions of Nonferrous Metals Society of China, 2020, 30: 2424−2434.

[6]     AZARIAN N, KHOEI S M M, Characteristics of a multi-component MgO-based bioceramic coating synthesized in-situ by plasma electrolytic oxidation [J]. Journal of Magnesium and Alloys, 2021, 9: 1595−1608.

[7]     SHI Zhi-ming, LIU Ming, ATRENS A. Measurement of the corrosion rate of magnesium alloys using Tafel extrapolation [J]. Corrosion Science, 2010, 52: 579−588.

[8]     CHEN Lian-xi, GUO Cheng, BLAWERT C, YANG Jun-jie, CHEN Dong-chu, WANG Xiao-jian, YU Zhen-tao, ZHELUDKEVICH M L, LI Wei. Evaluation of the biodegradation product layer on Mg−1Zn alloy during dynamical strain [J]. Journal of Magnesium and Alloys, 2021, 9: 1820−1833.

[9]     HE Jun-jie, JIANG Bin, XU Jun, ZHANG Jian-yue, YU Xiao-wen, LIU Bo, PAN Fu-sheng. Effect of texture symmetry on mechanical performance and corrosion resistance of magnesium alloy sheet [J]. Journal of Alloys and Compounds, 2017, 723: 213−224.

[10]    LIU Huan, JU Jia, YANG Xiao-wei, YAN Jing-li, SONG Dan, JIANG Jing-hua, MA Ai-bin. A two-step dynamic recrystallization induced by LPSO phases and its impact on mechanical property of severe plastic deformation processed $Mg_{97}Y_2Zn_1$ alloy [J]. Journal of Alloys and Compounds, 2017, 704: 509−517.

[11]    ZHANG Xin, LI Yong-jun, ZHANG Kui, WANG Chang-shun, LI Hong-wei, MA Ming-long, ZHANG Bao-dong. Corrosion and electrochemical behavior of Mg−Y alloys in 3.5% NaCl solution [J]. Transactions of Nonferrous Metals Society of China, 2013, 23: 1226−1236.

[12]    JIANG Shao-song, JIA Yong, WANG Xiao-jun. In-situ analysis of slip transfer and heterogeneous deformation in tension of Mg−5.4Gd−1.8Y−1.5Zn alloy [J]. Journal of Magnesium and Alloys, 2020, 8: 1186−1197.

[13]    BRIFFOD F, SHIRAIWA T, ENOKI M. Monotonic and cyclic anisotropies of an extruded Mg−Al−Ca−Mn alloy plate: Experiments and crystal plasticity studies [J]. Materials Science and Engineering A, 2020, 772: 138753.

[14]    YANG Qiang, LV Shu-hui, QIN Peng-fei, MENG Fan-zhi, QIU Xin, HUA Xi-ru, GUAN Kai, SUN Wei, LIU Xiao-juan, MENG Jian. Interphase boundary segregation induced phase transformation in a high-pressure die casting Mg−Al−La−Ca−Mn alloy [J]. Materials & Design, 2020, 190: 108566.

[15]    BHATTACHARYYA J J, SASAKI T T, NAKATA T, HONO K, KAMADO S, AGNEW S R. Determining the strength of GP zones in Mg alloy AXM10304, both parallel and perpendicular to the zone [J]. Acta Materialia, 2019, 171:

231−239.

[16] HUANG He, LIU Huan, WANG Ce, SUN Jia-peng, BAI Jing, XUE Feng, JIANG Jing-hua, MA Ai-bin. Potential of multi-pass ECAP on improving the mechanical properties of a high-calcium-content Mg−Al−Ca−Mn alloy [J]. Journal of Magnesium and Alloys, 2019, 7: 617−627.

[17] HOMAYUN B, AFSHAR A. Microstructure, mechanical properties, corrosion behavior and cytotoxicity of Mg−Zn−Al−Ca alloys as biodegradable materials [J]. Journal of Alloys and Compounds, 2014, 607: 1−10.

[18] SONG G L, ATRENS A. Corrosion mechanisms of magnesium alloys [J]. Advanced Engineering Materials, 1999, 1: 11−33.

[19] GRIMM M, LOHMÜLLER A, SINGER R F, VIRTANEN S. Influence of the microstructure on the corrosion behaviour of cast Mg−Al alloys [J]. Corrosion Science, 2019, 155: 195−208.

[20] NAM N D, MATHESH M, FORSYTH M, JO D S. Effect of manganese additions on the corrosion behavior of an extruded Mg−5Al based alloy [J]. Journal of Alloys and Compounds, 2012, 542: 199−206.

[21] ROBSON J D, HENRY D T, DAVIS B. Particle effects on recrystallization in magnesium-manganese alloys: Particle pinning [J]. Materials Science and Engineering A, 2011, 528: 4239−4247.

[22] PENG Jian, LV Bin-jiang, TONG Xiao-shan, PAN Fu-sheng. Current state and prospect of research on effects of Mn on the microstructure and properties in Mg−Zn serial magnesium alloys [J]. Light Metals, 2012, 8: 55−59.

[23] CHO D H, LEE B W, PARK J Y, CHO K M, PARK I M. Effect of Mn addition on corrosion properties of biodegradable Mg−4Zn−0.5Ca−xMn alloys [J]. Journal of Alloys and Compounds, 2017, 695: 1166−1174.

[24] YANG Jiang, PENG Jian, NYBERG E A, PAN Fu-sheng. Effect of Ca addition on the corrosion behavior of Mg−Al−Mn alloy [J]. Applied Surface Science, 2016, 369: 92−100.

[25] ZHANG Li, DENG Kun-kun, NIE Kai-bo, XU Fang-jun, SU Kun, LIANG Wei. Microstructures and mechanical properties of Mg−Al−Ca alloys affected by Ca/Al ratio [J]. Materials Science and Engineering A, 2015, 636: 279−288.

[26] KIM K H, NAM N D, KIM J G, SHIN K S, JUNG H C. Effect of calcium addition on the corrosion behavior of Mg−5Al alloy [J]. Intermetallics, 2011, 19: 1831−1838.

[27] VALIEV R Z, LANGDON T G. Principles of equal-channel angular pressing as a processing tool for grain refinement [J]. Progress in Materials Science, 2006, 51: 881−981.

[28] CAO Yang, NI Song, LIAO Xiao-zhou, SONG Min, ZHU Yun-tian. Structural evolutions of metallic materials processed by severe plastic deformation [J]. Materials Science and Engineering R: Reports, 2018, 133: 1−59.

[29] SUN Jia-peng, YANG Zhen-quan, HAN Jing, LIU Huan, SONG Dan, JIANG Jin-hua, MA Ai-bin. High strength and ductility AZ91 magnesium alloy with multi-heterogenous microstructures prepared by high-temperature ECAP and short-time aging [J]. Materials Science and Engineering A, 2018, 734: 485−490.

[30] WANG H L, XIANG Y T, LI Q Y, WANG X P, LIU Z C, HAO S S, LIU X, LIU L L, WANG G H, WANG D G,

ZHANG P A, BAO A Y, CHIU H F K, UNGVARI G S, LAI K Y C, BUCHANAN R W. The effect of artemether on psychotic symptoms and cognitive impairment in first-episode, antipsychotic drug-naive persons with schizophrenia seropositive to Toxoplasma gondii [J]. Journal of Psychiatric Research, 2014, 53: 119−124.

[31] LIU Huan, HUANG He, YANG Xiao-wei, LI Cheng, YAN Jing-li, JIANG Jing-hua, MA Ai-bin. Microstructure and mechanical property of a high-strength Mg−10Gd−6Y−1.5Zn−0.5Zr alloy prepared by multi-pass equal channel angular pressing [J]. Journal of Magnesium and Alloys, 2017 5: 231−237.

[32] LIU Huan, CHENG Zhao-jun, YAN Kai, YAN Jing-li, BAI Jing, JIANG Jing-hua, MA Ai-bin. Effect of multi-pass equal channel angular pressing on the microstructure and mechanical properties of a heterogeneous Mg88Y8Zn4 alloy [J]. Journal of Materials Science & Technology, 2016, 32: 1274−1281.

[33] ROSSI S, BONORA P L, PASINETTI R, BENEDETTI L, DRAGHETTI M, SACCO E. Laboratory and field characterization of a new sacrificial anode for cathodic protection of offshore structures [J]. Corrosion, 1998, 54: 1018−1025.

[34] WANG M, ZONG B Y, WANG G. Grain growth in AZ31 Mg alloy during recrystallization at different temperatures by phase field simulation [J]. Computational Materials Science, 2009, 45: 217−222.

[35] GE Q, MOSTAED E, ZANELLA C, YU Z T, VEDAN I M. Ultra-fine grained degradable magnesium for biomedical applications [J]. Rare Metal Materials and Engineering, 2014, 43: 2561−2566.

[36] HUANG He, LIU Huan, WANG Li-sha, YAN Kai, LI Yu-hua, JIANG Jing-hua, MA Ai-bin, XUE Feng, BAI Jing. Revealing the effect of minor Ca and Sr additions on microstructure evolution and mechanical properties of Zn−0.6Mg alloy during multi-pass equal channel angular pressing [J]. Journal of Alloys and Compounds, 2020, 844: 155923.

[37] ATRENS A, SONG G L, LIU M, SHI Z M, CAO F Y, DARGUSCH M S. Review of recent developments in the field of magnesium corrosion [J]. Advanced Engineering Materials, 2015, 17: 400−453.

[38] JIN Y M, BLAWERT C, YANG H, WIESE B, FEYERABEND F, BOHLEN J, MEI D, DENG M, CAMPOS M S, SCHARNAGL N, STRECKER K, BODE J, VOGT C, ROMER R W. Microstructure-corrosion behaviour relationship of micro-alloyed Mg−0.5Zn alloy with the addition of Ca, Sr, Ag, In and Cu [J]. Materials & Design, 2020, 195: 108980.

[39] WANG Ce, MA Ai-bin, SUN Jia-peng, ZHUO Xiao-ru, HUANG He, LIU Huan, YANG Zhen-quan, JIANG Jing-hua. Improving strength and ductility of a Mg−3.7Al−1.8Ca−0.4Mn alloy with refined and dispersed Al2Ca particles by industrial-scale ECAP processing [J]. Metals, 2019, 9: 767.

[40] WANG Ce, MA Ai-bin, SUN Jia-peng, LIU Huan, HUANG He, YANG Zhen-quan, JIANG Jing-hua. Effect of ECAP process on as-cast and as-homogenized Mg−Al−Ca−Mn alloys with different Mg2Ca morphologies [J]. Journal of Alloys and Compounds, 2019, 793: 259−270.

[41] LIU Huan, SUN Chao, WANG Ce, LI Yu-hua, BAI Jing, XUE Feng, MA Ai-bin, JIANG Jing-hua. Improving toughness of a $Mg_2Ca$-containing Mg−Al−Ca−Mn alloy via refinement and uniform dispersion of $Mg_2Ca$ particles [J]. Journal of Materials Science & Technology, 2020, 59: 61−71.

[42] MINGO B, MOHEDANO M, BLAWERT C, OLMO R D, HORT N, ARRABAL R. Role of Ca on the corrosion resistance of Mg−9Al and Mg−9Al−0.5Mn alloys [J]. Journal of Alloys and Compounds, 2019, 811: 151992.

[43] BAHMANI A, ARTHANARI S, SHIN K. Corrosion behavior of Mg−Mn−Ca alloy: Influences of Al, Sn and Zn [J]. Journal of Magnesium and Alloys, 2019, 7: 38−46.

[44] SHI Ying-chun, PENG Chao-qun, FENG Yan, WANG Ri-chu, WANG Nai-guang. Microstructure and electrochemical corrosion behavior of extruded Mg−Al−Pb−La alloy as anode for seawater-activated battery [J]. Materials and Design, 2017, 124: 24−33.

[45] WU Peng-peng, XU Fang-jun, DENG Kun-kun, HAN Fu-yin, ZHANG Zhong-zhong, GAO Rui. Effect of extrusion on corrosion properties of Mg−2Ca−$\chi$Al ($\chi$=0, 2, 3, 5) alloys [J]. Corrosion Science, 2017, 127: 280−290.

[46] GONG Chang-wei, HE Xin-ze, FANG Da-qing, LIU Bao-sheng, YAN Xue. Effect of second phases on discharge properties and corrosion behaviors of the Mg−Ca−Zn anodes for primary Mg-air batteries [J]. Journal of Alloys and Compounds, 2021, 861: 158493.

[47] SONG Ying-wei, SHAN Da-yong, CHEN Rong-shi, HAN En-hou. Effect of second phases on the corrosion behaviour of wrought Mg−Zn−Y−Zr alloy [J]. Corrosion Science, 2010, 52: 1830−1837.

[48] SONG Ying-wei, HAN En-hou, SHAN Da-yong, YIM C D, YOU B S. The role of second phases in the corrosion behavior of Mg−5Zn alloy [J]. Corrosion Science, 2012, 60: 238−245.

[49] ZHANG C, WU L, HUANG G S, HUANG Y, JIANG B, ATRENS A, PAN F S. Effect of microalloyed Ca on the microstructure and corrosion behavior of extruded Mg alloy AZ31 [J]. Journal of Alloys and Compounds, 2020, 823: 153844.

[50] LIAO J S, HOTTA M, MORI Y. Improved corrosion resistance of a high-strength Mg−Al−Mn−Ca magnesium alloy made by rapid solidification powder metallurgy [J]. Materials Science and Engineering A, 2012, 544: 10−20.

[51] ZHANG Jian-yue, JIANG Bin, YANG Qing-shan, HUANG Dan, TANG Ai-tao, PAN Fu-sheng, HAN Qing-you. Role of second phases on the corrosion resistance of Mg−Nd−Zr alloys [J]. Journal of Alloys and Compounds, 2020, 849: 156619.

[52] AUNG N N, ZHOU W. Effect of grain size and twins on corrosion behaviour of AZ31B magnesium alloy [J]. Corrosion Science, 2010, 52: 589−594.

[53] XU Hong, ZHANG Xin, ZHANG Kui, SHI Yang, REN Ji-ping. Effect of extrusion on corrosion behavior and corrosion mechanism of Mg−Y alloy [J]. Journal of Rare Earths, 2016, 34: 315.

[54] YANG J, PENG J, NYBERG E, PAN F S. Effect of Ca addition on the corrosion behavior of Mg−Al−Mn alloy [J]. Applied Surface Science, 2016, 369: 92−100.

[55] LUO Yao-feng, DENG Yun-lai, GUAN Li-qun, YE Ling-ying, GUO Xiao-bin, LUO An. Effect of grain size and crystal orientation on the corrosion behavior of as-extruded Mg−6Gd−2Y−0.2Zr alloy [J]. Corrosion Science, 2020, 164: 108338.

# 含 Al₂Ca 相和 Mg₂Ca 相 Mg−Al−Ca−Mn 合金经等通道转角挤压加工后的腐蚀性能

何书恒 [1]，王 策 [2]，孙 超 [1]，张 越 [3]，严 凯 [4]，江静华 [1]，白 晶 [3]，薛 烽 [3]，刘 欢 [1,5]

1. 河海大学 力学与材料学院，南京 210000；2. 天津大学 材料科学与工程学院，天津 300350；
3. 东南大学 材料科学与工程学院，南京 211189；4. 扬州大学 机械工程学院，扬州 225127；
5. 南京云海特种金属股份有限公司 江苏省轻金属合金研究重点实验室，南京 211200

摘　要：为了研究 Al₂Ca 相和 Mg₂Ca 相对 Mg−Al−Ca−Mn 合金腐蚀行为的影响，采用金相显微镜、扫描电子显微镜、浸泡和电化学测试对仅含 Al₂Ca 相(2Ca)和仅含 Mg₂Ca 相(4Ca)的铸态及 ECAP 态合金进行研究。在腐蚀初期，两种铸态合金的腐蚀速度比 ECAP 合金的慢。随着腐蚀时间的延长，ECAP 合金的腐蚀程度变得比铸态合金轻微，这主要归因于 ECAP 合金中第二相的有效细化及分散。此外，2Ca 合金的腐蚀程度始终小于 4Ca 合金，表明 Al₂Ca 相比 Mg₂Ca 相更有利于提高 Mg−Al−Ca−Mn 合金的耐腐蚀性能。最后，根据合金腐蚀表面的形貌观察和电化学测试结果，对由 Al₂Ca 相和 Mg₂Ca 相的分布和形貌引起合金的不同腐蚀机理进行讨论。

关键词：Mg−Al−Ca−Mn 合金；等通道转角挤压；第二相；细化；腐蚀性能

**(Edited by Bing YANG)**